Effect of Yttrium on Iron-Rich Phases and Mechanical Properties of As-Cast Al-Fe Alloy with Low Si Concentration

Wenjie Wu , Wenxia Lai , Ziteng Cao , Chengdong Li * , Mei Zhao *

Posted Date: 19 December 2025

doi: 10.20944/preprints202512.1715.v1

Keywords: Al-Fe alloy; iron-rich phases; Y rare earth; microstructure; mechanical properties

 doi:10.20944/preprints202512.1715.v1

Article

Effect of Yttrium on Iron-Rich Phases and Mechanical Properties of As-Cast Al-Fe Alloy with Low Si Concentration

Wenjie Wu, Wenxia Lai, Ziteng Cao, Chengdong Li * and Mei Zhao *

College of Materials Science and Engineering, Qingdao University of Science and Technology, Qingdao 266000, China
* Correspondence: lichengdong@qust.edu.cn (C.L.); zhaomei@qust.edu.cn (M.Z.)

Abstract

In Al–Fe alloys, the mechanical performance is determined by the morphology of iron-rich phases. In this work, AA8176(Al-1Fe)- nY (n = 0, 0.3, 0.5, 0.7, and 0.9 wt.%) alloys were prepared by the cast method. To systematically analyze the influence of Y on microstructure evolution and tensile behavior, a multi-scale characterization approach was employed, combining metallography, electron microscopy, X-ray diffraction, cooling curve analysis, and tensile tests. The results revealed that the optimal refinement effect was achieved when the amount of Y content was 0.5 wt.%. The microstructure of the alloy was significantly modified by Y addition. The coarse needle-like $Al_{13}Fe_4$ phases were gradually transformed into short rod-like and particle morphology. And the average length was decreased from 10.01 μm to 2.65 μm. Meanwhile, some small size $Al_{10}Fe_2Y$ phases were formed around the $Al_{13}Fe_4$ phases. Additionally, the secondary dendrite arm spacing (SDAS) of A8176 alloy was reduced from 31.33 μm to 20.24 μm. Furthermore, the mechanical properties of the AA8176 alloy were improved due to the modified microstructure. The tensile strength of the alloy was increased from 84.47 MPa to 96.86 MPa, and the elongation was increased from 18.6 % to 23.1 %. It is proposed that the growth of α-Al dendrite and $Al_{13}Fe_4$ phases were effectively inhibited by segregation of Y atoms around α-Al dendrite and $Al_{13}Fe_4$ phases during solidification. And the $Al_{10}Fe_2Y$ phases were formed by these Y atoms with Al and Fe elements. However, the formation of coarse $Al_{10}Fe_2Y$ phases was promoted by excessive Y content, which resulting in a substantial degradation in mechanical properties.

Keywords: Al-Fe alloy; iron-rich phases; Y rare earth; microstructure; mechanical properties

1. Introduction

For Al-Fe-based aluminum alloys, excellent heat and wear resistance are achieved, and the high specific strength and low density of aluminum alloys was maintained [1–3]. The advantages of Al-Fe-based alloys are predominantly derived from various iron-rich phases (formed by Fe, Al, and other alloying elements such as Si, Mg, Mn) during solidification and heat treatment processes, which is attributed to the intentional addition of Fe [4,5]. Among these alloying elements, Si plays the most important role in determining the types of iron-rich phases. In the Al-Fe alloy with high Si content, the iron-rich phases are mainly consisted of α-AlFeSi (Al_8Fe_2Si) and β-AlFeSi (Al_5FeSi). In contrast, in the Al-Fe alloy with low Si content, the iron-rich phases are consisted of $Al_{13}Fe_4$ (Al_3Fe), Al_6Fe, and Al_mFe phases [6].

Owing to the extremely low solubility of Fe in the Al matrix, a sharp increase in the size of iron-rich phases is achieved when the Fe content exceeds 0.1 wt.%. And their morphologies are gradually transformed from fine fibrous to large needle-like, flake-like, and plate-like [7,8]. These coarse iron-rich phases act as crack initiation sites, which led to stress concentration during plastic

 doi:10.20944/preprints202512.1715.v1

deformation and thereby deteriorate the alloy's mechanical performance. Furthermore, the flow of melt is hindered by coarse iron-rich phases precipitated in the solidification, consequently inducing casting defects [9]. Therefore, it is essential to develop effective methods for modifying the morphology of iron-rich phases in Al-Fe aluminum alloys.

The 8000 series aluminum alloys, including AA8076, AA8079, AA8176 and other grades, belong to Al-Fe aluminum alloys with low Si concentration, which are mainly used in packaging, containers, cables and other fields. Currently, research on the refinement of iron-rich phases in such low-Si Al-Fe alloys remains insufficient.

Some strategies such as rapid solidification [10], mechanical alloying [11], applied magnetic field [12], and severe plastic deformation [13,14] have been employed to modify the iron-rich phases in aluminum alloys. However, for these methods, stringent equipment conditions and entail higher costs are required, which limit their applicability in industrial production.

In comparison to several refiner such as Mn, Ti, Ni, and Cr, the addition of rare earth metals, including La, Ce, Er, Sc, and Sm are more attractive for aluminum casting alloys [15–25]. When these rare earth elements are used, the microstructure is modified and the mechanical properties is improved. Meanwhile, the melt is purified, and the content of gases and inclusions are reduced [26]. During these rare earth elements, the widespread application of high-value rare earth elements such as Er, Sc, and Sm in large-scale aluminum alloy manufacturing is frequently hindered by the high costs. Additionally, in comparison to rare earth elements such as La and Ce, Y tends to be easier to combine with Fe in Al-Fe alloys to form Al-Fe-Y ternary phases [27–29]. On the one hand, a portion of Fe atoms are consumed by the formation of the Al-Fe-Y ternary phases, thereby reducing the volume fraction of needle-like iron-rich phases. On the other hand, more favorable morphologies are typically exhibited by the Al-Fe-Y ternary phases, which results in an increase in the number of strengthening secondary phases.

The beneficial effect of Y addition on both the microstructure and the mechanical properties of aluminum alloys has been demonstrated by several studies [30,31]**.** Ding et al. [32] reported that a significant refinement effect on 6063 aluminum alloy was achieved by Y addition. The size of Mg_2Si particles was reduced by the addition of Y, and the β-AlFeSi phases were transformed into the α-AlFeSi phases. Furthermore, both tensile strength and elongation of the AA6063 alloy were improved by the combined addition of Y and the Al–Ti–B master alloy. Liu et al [33]. found that the microstructure of as-cast ADC12 aluminum alloy was significantly refined by Y addition, resulting in a notable increase in the average size of the α-Al phase, as well as the coarse Si and iron-rich phases. And the mechanical properties of the ADC12 aluminum alloy were notably enhanced by the combination of Y addition and heat treatment. Wan et al [34]. reported on the effects of adding different contents of Y on the microstructure and tensile properties of recycled A356 cast alloy. When the Y content was 0.3 wt.%, the average length of the β-Fe phases was reduced from 78 μm to 20 μm and the finest α-Al phases were obtained. Meanwhile, the eutectic silicon was fully modified in morphology.

The comprehension of Y modification for coarse iron-rich phases was enhanced by these reports. However, limited attention has been paid to the addition of Y in Al-Fe aluminum alloys with low Si concentration. Consequently, the underlying modification mechanism and the associated mechanical property response need to be further studied.

As described above, AA8176 was selected as the matrix material and Y was utilized as the refiner in this study to explore effective approaches for refining iron-rich phases in Al-Fe alloys with low Si concentration. Y was added to AA8176 alloys by the cast method. The influence of varying Y additions (0, 0.3, 0.5, 0.7, and 0.9 wt.%) on the evolution of the iron-rich phases, α-Al dendrite, and mechanical properties of as-cast AA8176 alloys were systematically studied. The aim of this study is to reveal the refinement mechanism of Y on the microstructure and the strengthening mechanism of mechanical properties of AA8176 aluminum alloys, and to propose a new strategy for achieving effective refinement of iron-rich phases in Al-Fe alloys with low Si concentration.

 doi:10.20944/preprints202512.1715.v1

2. Materials and Methods

AA8176 alloy samples with varying Y additions (0, 0.3, 0.5, 0.7, and 0.9 wt.%) were fabricated using pure aluminum ingots (≥99.7 wt.%), Al-20 wt.% Fe master alloy, and Al-20 wt.% Y master alloy. The cast process was as follows: (1) Purity Al ingots, and Al-20 wt.% Fe were melted in furnace at 760 °C; (2) A suitable quantity of Al-20 wt.% Y master alloy was added at 730℃ and held for 15 min after addition;(3) The temperature of furnace was reduced to 720 °C for degassing and slag removal to obtain a purified melt ;(4) The molten alloy was subsequently poured into a steel mold, thus producing the experimental cast samples for further analysis. Before the aluminum alloy was poured, the mold was placed in a muffle furnace for preheating, with the temperature set to 250°C. The composition of the experimental alloys was determined using a direct reading spectrometer, as presented in Table 1.

Table 1. Chemical composition of aluminum alloy samples (wt.%).

Alloy	Fe	Y	Si	Al
AA8176	1.02	<0.01	<0.05	Bal.
03Y	1.09	0.29	<0.05	Bal.
05Y	1.04	0.52	<0.05	Bal.
07Y	0.98	0.68	<0.05	Bal.
09Y	1.01	0.91	<0.05	Bal.

To systematically analyze the effects of Y addition on the microstructural evolution and mechanical properties of AA8176 aluminum alloy, a comprehensive set of experimental procedures was established. The sizes of specimens for metallographic observation and tensile test are shown in Figure 1. And the Samples for metallographic observation were cut from the tensile test specimens, with the sampling location illustrated in Figure 1. Before the metallographic observation, the samples were sequentially mechanically ground with SiC sandpapers of #180, #400, #800, #1200and #2000, and subsequently followed by polishing with diamond paste to achieve a mirror-like surface finish. After that the samples were etched with a solution of Keller's reagent (2.5 mL HNO_3+1.0 mL HF+1.5 mL HCl+95 mL H_2O) for 10 s.

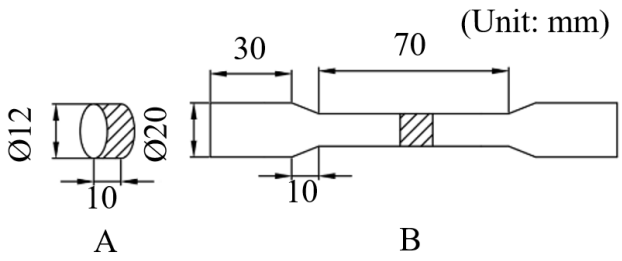

Figure 1. Schematic of (A) microstructure observation and (B) tensile test specimen.

Metallographic observations were carried out using an XJP-200(Nanjing Jiangnan Optoelectronics Co. Ltd., Nanjing, China) inverted optical microscope. The SDAS of alloys were measured by the line intercept method using Image-Pro Plus software. Phase analysis was performed with X-ray diffractometer using a D/MAX-2500/PC X-ray diffractometer (Rigaku, Tokyo, Japan) equipped with a Cu Kα radiation source. The diffraction patterns were recorded over a 2θ range of 20° to 90° at a scanning speed of 5°/min. The microstructure and fracture morphology observation were conducted using Regulus8100 field emission scanning electron microscope (HITACHI, Tokyo, Japan). The $Al_{13}Fe_4$ and $Al_{10}Fe_2Y$ phases were further characterized by FEI Tecnai F20 transmission electron microscopy (FEI Company, Hillsboro, America). The samples for TEM observation were prepared using automatic twinjet electropolisher. The cooling curves of the alloy during solidification

 doi:10.20944/preprints202512.1715.v1

were measured using a THMA010K temperature recorder (TengHui, Yuyao, China) coupled with a K-type thermocouple inserted into the melt center to ensure reliable temperature monitoring throughout solidification. Tensile tests were conducted on an AI-700 tensile testing machine (Gotech, Taiwan, China) at room temperature with a tensile speed of 5 mm·min^{-1}. As shown in Figure 1, the bone-shaped specimens were used for tensile property testing, with five tests conducted for each composition.

3. Results

3.1. The Microstructure of AA8176-xY

3.1.1. Metallographic Observation

The microstructures of as-cast AA8176 aluminum alloys with varying Y contents were characterized using optical microscopy, as presented in Figure 2(a-d). The microstructure of unmodified AA8176 alloy is predominantly composed of α-Al and eutectic structure [35]. As shown in Figures 2(a) and 3(a), the eutectic iron-rich phases in the unmodified AA8176 alloys predominantly exhibited coarse needle-like morphology with an average length of 10.01 μm. These coarse needle-like iron-rich phases were located along grain boundaries. And the stress concentration during plastic deformation is greatly promoted by these coarse needle-like iron-rich phases, leading to a decline in the mechanical properties.

With the Y content increasing from 0 wt.% to 0.5 wt.%, significant changes in the morphology of the iron-rich phases were observed. The average length of the iron-rich phases was decreased from 10.01 μm to 2.65 μm, transforming into short rod-like and particulate morphologies as shown in Figures 2(b-c) and 3(a). When the Y content was further increased to 0.7 wt.%, the average length of iron-rich phases exhibited an increasing trend as illustrated in Figure 2(d). When the Y content was 0.9wt.%, the average length of iron-rich phases was significantly increased to 7.87 μm, as shown in Figures 2(e) and 3(a). Concurrently, a notable increase in the number of secondary phases within the alloy was observed.

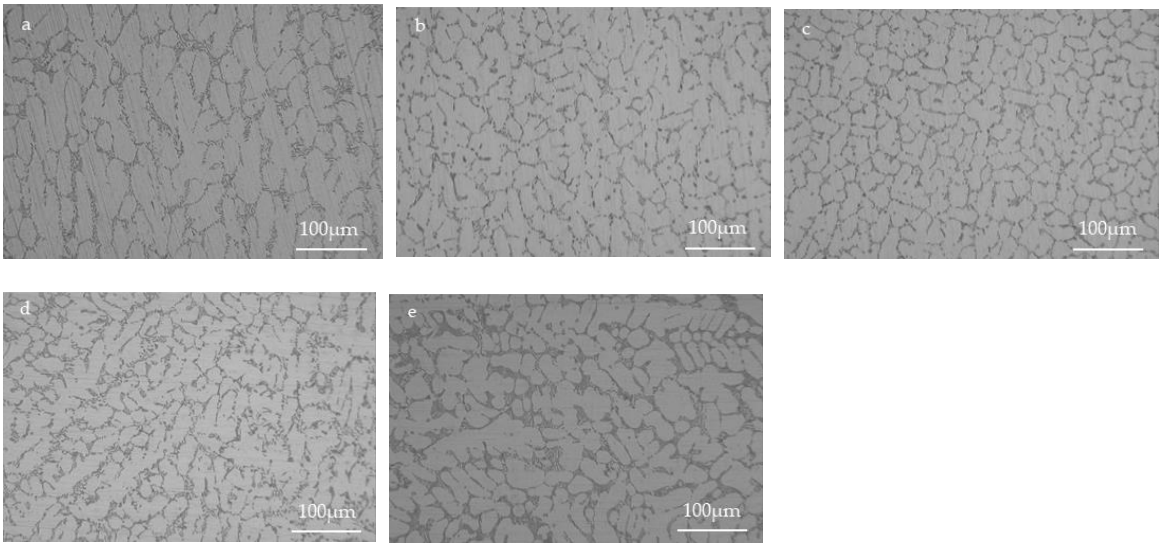

Figure 2. OM images of as-cast AA8176 alloys with different Y contents: (a) AA8176; (b) Alloy 03Y; (c) Alloy 05Y; (d) Alloy 07Y; (e) Alloy 09Y.

 doi:10.20944/preprints202512.1715.v1

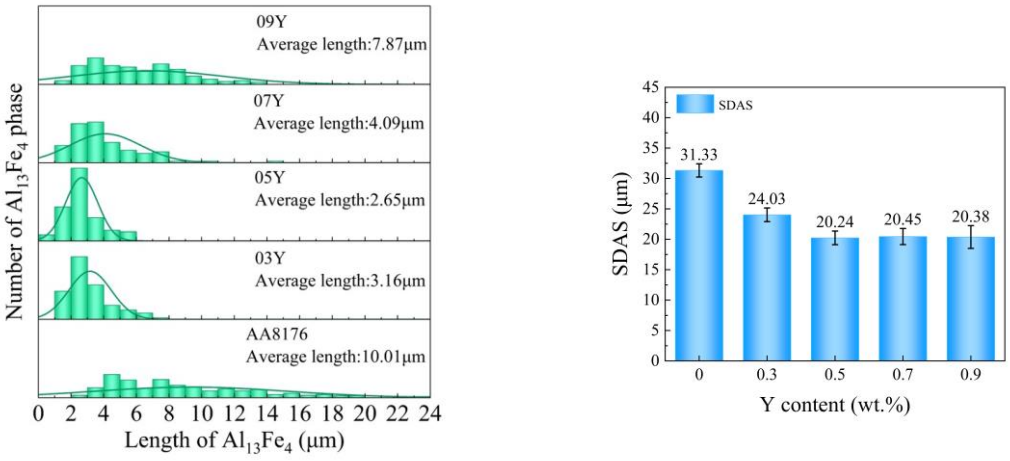

(**a**) (**b**)

Figure 3. (a) Distribution of the length of iron-rich phases in as-cast AA8176 alloys with different Y contents; (b) SDAS of AA8176 alloys with different Y contents.

To further analyze the impact of Y addition on the microstructure of AA8176 alloy, the SDAS of the α-Al matrix was measured for all alloys using the line intercept method in Image-Pro Plus software. For the unmodified AA8176 alloy, the α-Al dendric was relatively coarse, corresponding to an SDAS value of approximately 31.33 μm as shown in Figure 3(b). With the Y addition to AA8176 alloys, the SDAS values of the Alloy 03Y, Alloy 05Y, Alloy 07Y, and Alloy 09Y were 24.03 μm, 20.24 μm, 20.45 μm, and 20.38 μm, respectively. It is confirmed by these results that the addition of Y promotes the refinement of both the iron-rich phases and the α-Al dendritic structure. Notably, no further enhancement in the refinement effect of Y on α-Al was observed when the Y content exceeded 0.5 wt.%.

3.1.2. SEM and XRD Pattern

Figure 4 and Table 2 display SEM images and corresponding EDS analysis results for the AA8176 alloys with different Y contents. According to the X-ray diffraction patterns shown in Figure 6, except for α-Al, the presence of the $Al_{13}Fe_4$ phases was detected in all AA8176 alloys with different Y contents, which is consistent with the reference code from the Joint Committee on Powder Diffraction Standards (JCPDS) Card No. 29-0042 reference code [36].

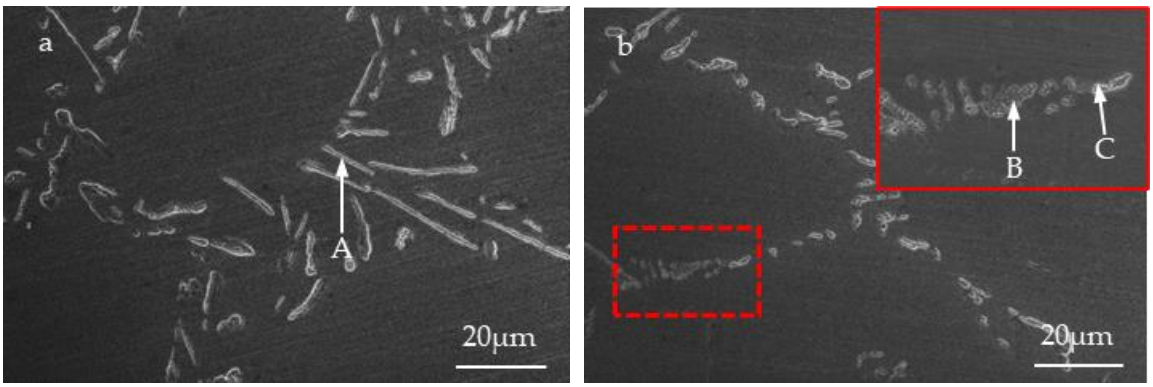

 doi:10.20944/preprints202512.1715.v1

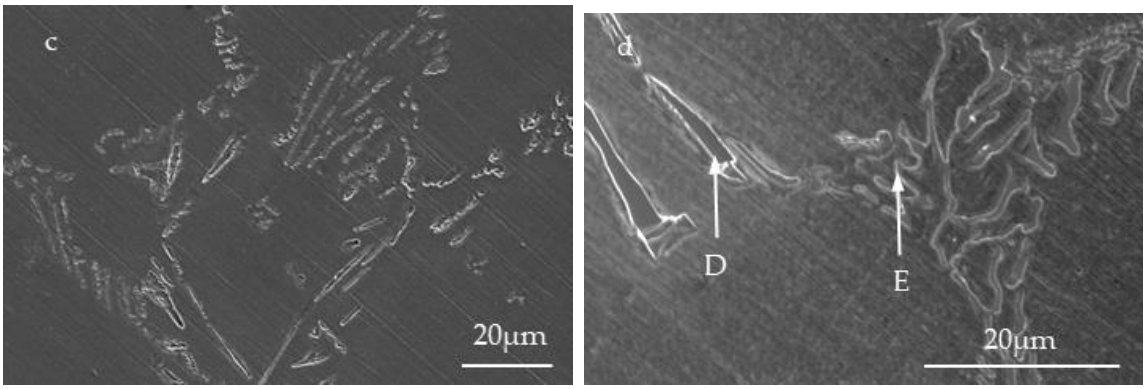

Figure 4. SEM images of as-cast AA8176 alloys with different Y contents:(a) AA8176; (b) Alloy 05Y; (c) Alloy 09Y. (d) Extremely coarse $Al_{13}Fe_4$ and $Al_{10}Fe_2Y$ phases in Alloy 09Y.

Table 2. Composition of aluminum alloy samples (wt.%).

Point	Al K	Fe K	Y K	Possible phase
A	74.44	25.56	—	$Al_{13}Fe_4$
B	89.90	6.49	3.61	$Al_{10}Fe_2Y$
C	78.12	21.88	—	$Al_{13}Fe_4$
D	76.82	23.72	—	$Al_{13}Fe_4$
E	84.21	9.70	6.09	$Al_{10}Fe_2Y$

As illustrated in Figure 4(a), the microstructure of the as-cast AA8176 alloy was primarily composed of α-Al matrix and coarse needle-like $Al_{13}Fe_4$ phases distributed along the grain boundaries. When the Y content was increased to 0.5 wt.%, the iron-rich phases were refined into short rod-like and particulate morphologies instead of the coarse needle-like structures, as shown in Figure 4(b). Furthermore, EDS results for points B and C (Table 2) indicated the presence of Al-Fe-Y ternary phases attached to $Al_{13}Fe_4$ phases in the Alloy 05Y. In contrast, when the Y content exceeded 0.5 wt.%, the refinement efficiency of Y was diminished. As shown in Figure 4(c), the average length of iron-rich phases in Alloy 09Y were increased, with an increase in both the quantity and size of the Al-Fe-Y ternary phases. Moreover, as illustrated in Figure 4(d), a morphology characterized by the aggregation of extremely coarse $Al_{13}Fe_4$ and $Al_{10}Fe_2Y$ phases was observed. The formation of these Al-Fe-Y ternary phases around the coarse $Al_{13}Fe_4$ phases was confirmed by EDS results from points E and F (Table 2).

According to the XRD patterns in Figure 5, the $Al_{10}Fe_2Y$ phases were detected in the Alloy 05Y, Alloy 07Y, and Alloy 09Y, which is consistent with the JCPDS Card No.53-0532 reference code [37]. Furthermore, in the XRD pattern of Alloy 09Y, the peak intensity of $Al_{10}Fe_2Y$ phases was increased, while that of $Al_{13}Fe_4$ phases was decreased. This trend is mainly attributed to the consumption of Fe atoms by the formation of coarse $Al_{10}Fe_2Y$ phases, which results in a reduction of Fe available for $Al_{13}Fe_4$ phases precipitation. Based on the elemental ratios obtained from EDS and XRD patterns, the Al-Fe-Y ternary phases observed in the SEM images (Figure 4) are most likely to be the $Al_{10}Fe_2Y$ phases.

 doi:10.20944/preprints202512.1715.v1

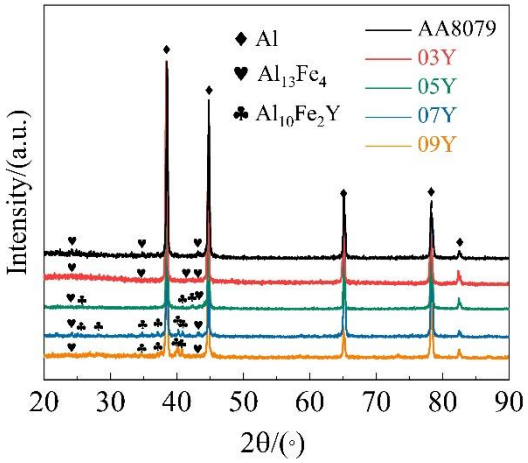

Figure 5. XRD patterns of the AA8176 alloys with different Y contents.

3.1.3. TEM Observation

Initial morphological characterization and EDS analysis were conducted on the secondary phases possibly containing Fe and Y elements in Alloy 05Y, as indicated by earlier SEM observations. Notably, the enrichment of Y elements around the surface of the $Al_{13}Fe_4$ phases and Al-Fe-Y ternary phases are formed with Al and Fe elements were clearly revealed by the Y mapping, as shown in Figure 6(d).

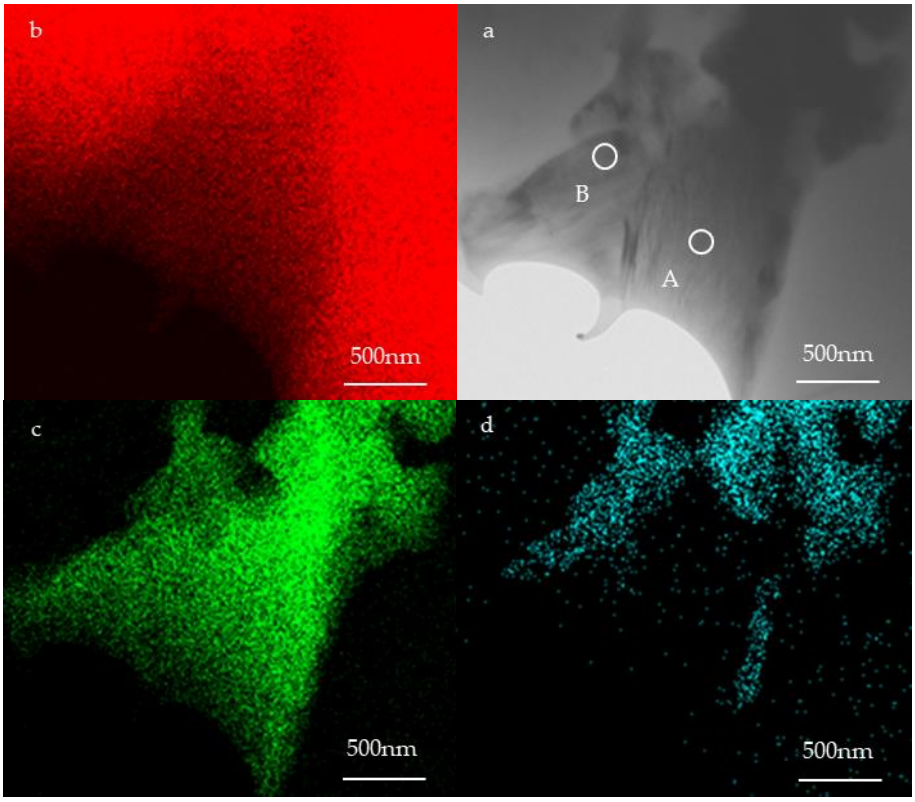

 doi:10.20944/preprints202512.1715.v1

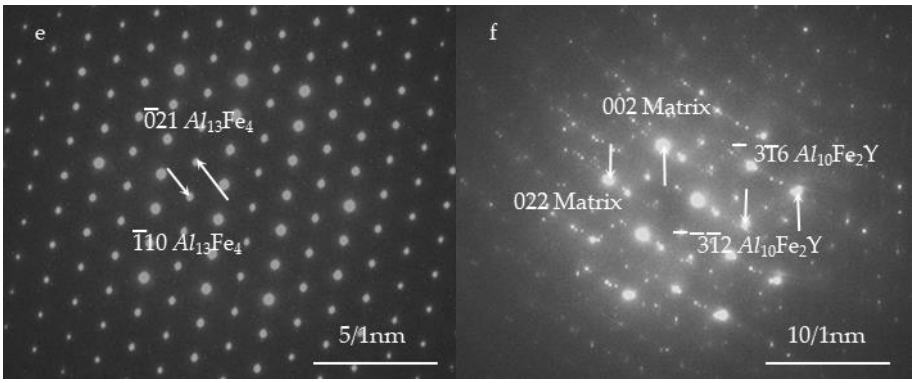

Figure 6. TEM characterization of the as-cast Alloy 05Y: (a): TEM bright-field image of Alloy; (b–d): EDS mapping results of $Al_{13}Fe_4$ phase and $Al_{10}Fe_2Y$ phase; (e) and (f): SAED patterns in the selected areas A and B, respectively.

To further identify the crystal structure of these phases, SAED patterns were collected from point A (corresponding to $Al_{13}Fe_4$ phases) and point B (corresponding to Al-Fe-Y ternary phases), as shown in Figure 6(e) and (f), respectively. The SAED pattern acquired at point A can be indexed to the $Al_{13}Fe_4$ phases. Due to the greater sample thickness at point B, the SAED pattern obtained from this location contained contributions from more than one kind phase, which was confirmed to consist mainly of α-Al matrix and $Al_{10}Fe_2Y$ phase, as illustrated in Figure 6(f).

3.1.4. Cooling Curves

The cooling curves and differential curves for AA8176 alloy, Alloy 05Y and Alloy 09Y are shown in Figure 8 and the characteristic temperatures of the eutectic reaction summarized in Table 3. T_{EN}, T_{EU}, and T_{EG} denote the eutectic nucleation temperature, eutectic minimum undercooling temperature and eutectic growth temperature, respectively. According to the Al-Fe alloy binary phase diagram, the eutectic temperature of Al-Fe alloys is approximately 655 °C [38], which is consistent with the characteristic values measured for the AA8176 alloy. With the addition of 0.5 wt.% Y, T_{EN} was decreased to 649.9 ℃ and T_{EG} was decreased to 643.6 ℃, respectively, indicating the adsorption and hindering effects of Y during the nucleation and growth processes of $Al_{13}Fe_4$ eutectic phases [39]. Additionally, a new peak emerged in the cooling curve, with a nucleation temperature around 626.8 °C, corresponding to the nucleation and growth of the $Al_{10}Fe_2Y$ phases [40]. When the Y content was increased to 0.9 wt.%, only minor changes were detected on the values of both T_{EN} and T_{EG}, indicating the adsorption and hindering effects of Y on the eutectic structure were not further enhanced. In contrast, the T'_{EN} of Alloy 09Y was significantly increased, suggesting that the nucleation and growth of $Al_{10}Fe_2Y$ phases were greatly promoted by higher Y content. This also account for the presence of numerous coarse $Al_{10}Fe_2Y$ phases in Alloy 09Y.

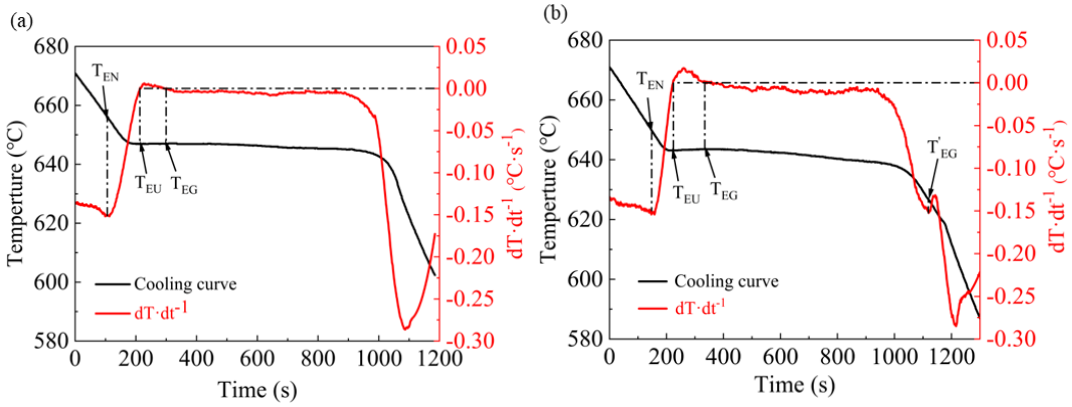

 doi:10.20944/preprints202512.1715.v1

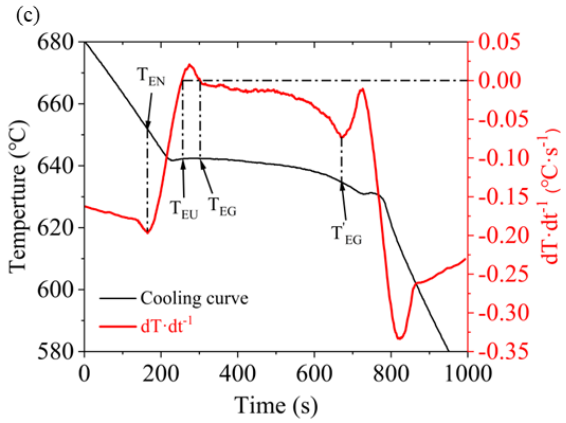

Figure 7. Cooling curves of (a): AA8176; (b): Alloy 05Y; (c): Alloy 09Y.

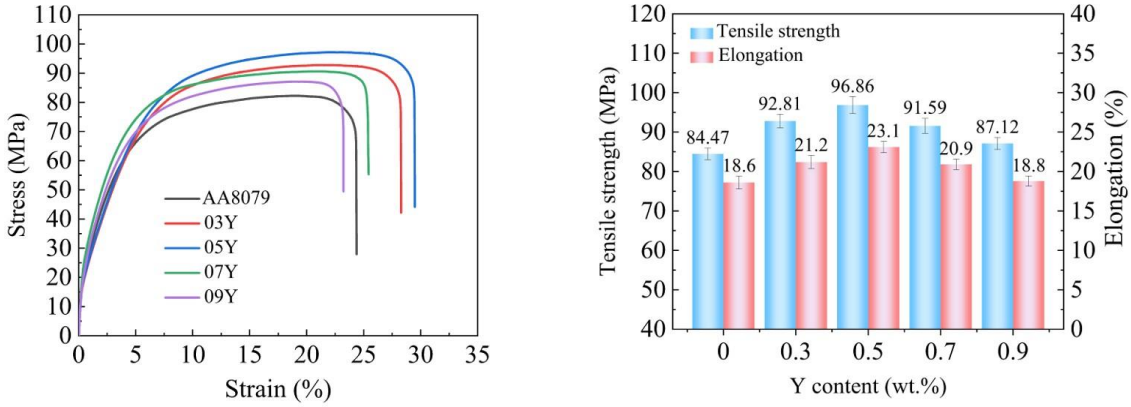

(**a**) (**b**)

Figure 8. (a) Engineering stress–strain curves (b) Mechanical properties of AA8176 alloys with different Y contents.

Table 3. Characteristic values of eutectic reaction.

Alloy	T_{EN} (℃)	T_{EU} (℃)	T_{EG} (℃)	T'_{EN} (℃)
AA8176	656.2	646.9	647.0	—
Alloy 05Y	649.9	643.1	643.5	626.8
Alloy 09Y	651.1	642.6	642.9	634.7

3.2. Mechanical Property

The mechanical properties of cast AA8176 alloys with different Y contents are presented in Figure 8. In unmodified AA8176 alloy, the ultimate tensile strength of the alloy was 84.47 MPa and the elongation was 18.6 %. Optimal mechanical properties were achieved when the Y content was increased to 0.5 wt.%. The ultimate tensile strength was increased to 96.86 MPa and elongation was increased to 23.1 %. However, further increase in Y content to 0.9 wt.% led to a reduction in both ultimate tensile strength and elongation. Therefore, it can be deduced that the ultimate tensile strength and the elongation of the AA8176 alloys exhibited a trend of firstly increasing and then decreasing with rising Y content.

Figure 9 presents the fracture surfaces of the as-cast AA8176 alloys with different Y contents. In the unmodified AA8176 alloy, shallow and irregularly sized dimples are observed, as shown in Figure 9(a). During tensile deformation, cracks were nucleated at the iron-rich phases and propagated along the interface between the iron-rich phases and the matrix. For Alloy 05Y, deeper and more uniformly distributed dimples were observed, with modified iron-rich phases observed within the dimples, as shown in Figure 9(c). However, when the Y content exceeded 0.5 wt.%, the weakening

 doi:10.20944/preprints202512.1715.v1

refinement effect of Y on the $Al_{13}Fe_4$ phases and formation of coarse $Al_{10}Fe_2Y$ phases resulted in a subsequent reduction in the ductility of the AA8176 alloys. Correspondingly, the fracture surfaces exhibited a tendency toward shallower dimples.

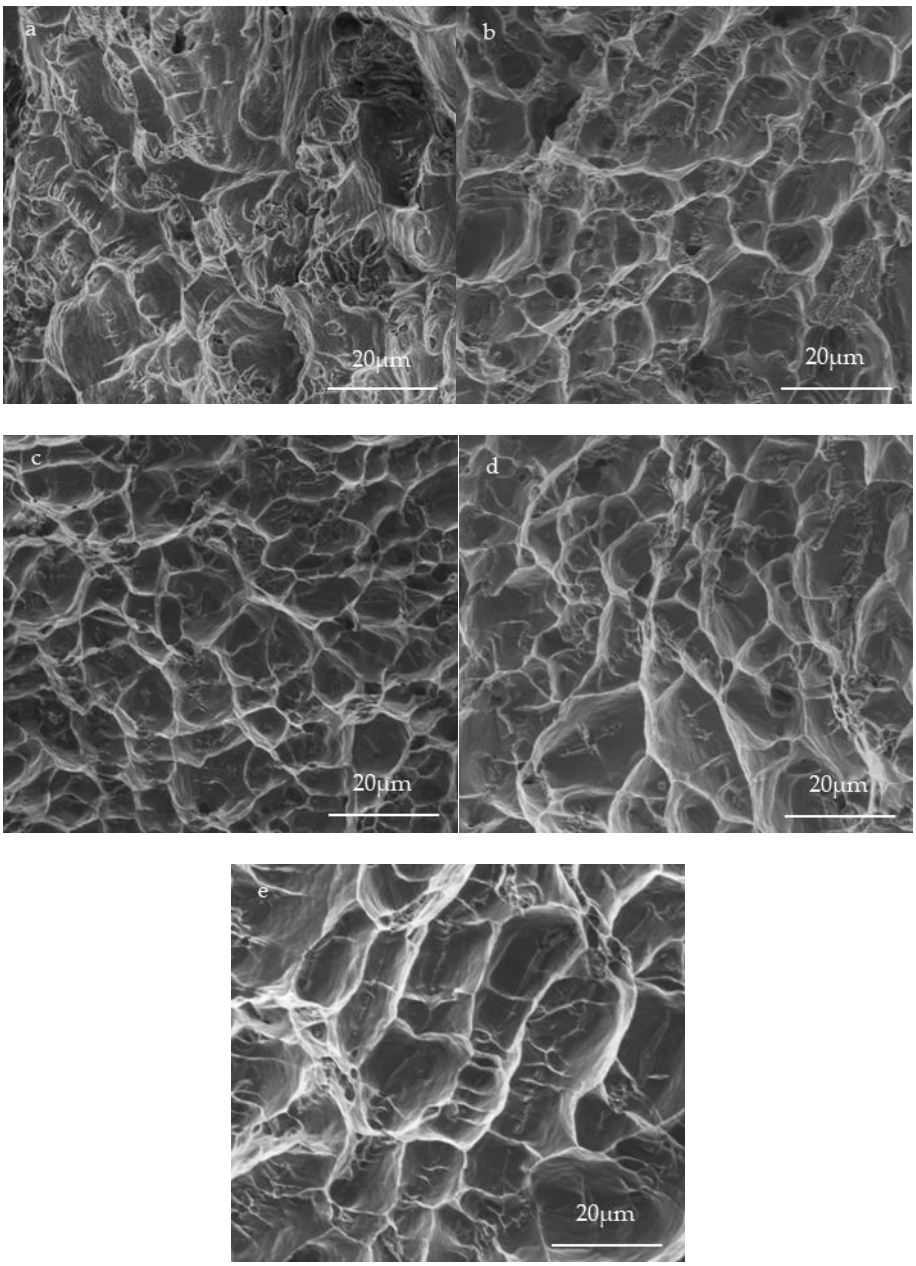

Figure 9. SEM image of tensile fracture morphology: (a) AA8176; (b) Alloy 03Y; (c) Alloy 05Y; (d) Alloy 07Y; (e) Alloy 09Y.

4. Discussion

4.1. Effect of Y Addition on α-Al Dendrite

As the total solid-liquid interface area between dendritic arms in the system is gradually decreased, neighboring dendritic arms are grown and merged, resulting in the formation of coarse dendritic structures during the solidification process. The atomic radius of the rare earth element Y and Al are 0.182 nm and 0.143 nm [33], respectively, indicating a difference of 27%. According to the Hume-Rothery rule, the formation of solid solutions is inhibited by a radius difference exceeding 15 % between solvent and solute [41].Consequently, extremely low solubility of Y element in Al matrix is exhibited (less than 0.035 mol.% at 573 K [42]), and enrichment of Y atoms at the dendritic fronts tends to occur during solidification.The growth and merging of dendritic arms are restricted by this

 doi:10.20944/preprints202512.1715.v1

enrichment, leading to a reduction in the SDAS of α-Al matrix [43]. The growth induced by element enrichment is described based on the growth restriction factor (GRF) as follows [18,44]:

$$GRF = C_Y \cdot \mathrm{m} \cdot (K - 1)$$

where C_Y is the concentration of solute Y in the alloy melt, m is the liquidus slope, and k is the equilibrium partition coefficient [18]. For the Al–Y alloy system, m=4.98 and k=0.5 are given by the Al–Y binary phase diagram. For the AA8176 alloy with 0.5 wt.%Y, the calculated GRF is approximately 1.25 K, the growth of α-Al is effectively inhibited by the addition of Y.

4.2. Effect of Y Addition on Iron-Rich Phases

The $Al_{13}Fe_4$ phases prefer to grow along the [010] orientation, resulting in the formation of coarse needle-like and plate-like morphologies during solidification [22]. The influence of active solute atoms on crystal growth is theoretically explained through doping (substitutional incorporation) and adsorption (surface segregation). There exists a significant difference in atomic radius between Y atoms and Al/Fe atoms—specifically, the atomic radius of Y, Al, and Fe are 0.182 nm, 0.143 nm, and 0.128 nm, respectively [33,45]. Owing to this remarkable size mismatch, Y atoms can't easily substitute Al or Fe atoms in the $Al_{13}Fe_4$ phases. According to result of EDS, rare Y element was detected in the eutectic $Al_{13}Fe_4$ phase, which directly confirms that the doping of Y atoms into $Al_{13}Fe_4$ phases is not the main mechanism for the refinement of $Al_{13}Fe_4$ phases. This experimental observation is consistent with the theoretical calculation results reported by Pang et al [29], which show that Y doping into $Al_{13}Fe_4$ phases increases their formation enthalpy. In contrast, the adsorption of Y on the (010) plane is an exothermic reaction, Y atoms are easily adsorbed on the (010) plane during the solidification process. The adsorption of Y atoms modifies the surface structure of the (010) plane and undermines the preferential growth along the [010] direction. In the final solidification stage, Y atoms eventually form $Al_{10}Fe_2Y$ ternary phases [29,40]. When the Y content reaches 0.9 wt.%, excessive aggregation of Y atoms significantly increases the nucleation temperature of the $Al_{10}Fe_2Y$ phases. The nucleation and growth of coarse $Al_{10}Fe_2Y$ phases leads to a massive consumption of Y atoms. This reduces the amount of Y atoms for inhibiting the preferential growth of the $Al_{13}Fe_4$ phases, resulting in a weakened refinement effect [18].

4.3. Strengthening Mechanism

Due to the extremely low solid solubility of Y and Fe in the Al matrix and the fact that the mechanical test specimens used in this study underwent no plastic deformation processing, solid solution strengthening and dislocation strengthening are not considered to be the primary mechanisms responsible for the enhancement in mechanical properties. Thus, the enhancement of ultimate tensile strength can be attributed to two factors. Firstly, $Al_{13}Fe_4$ intermetallic compounds are second phases with high hardness and brittleness, distributing on the a-Al matrix. During tensile process, deformation of the alloy is hindered by the $Al_{13}Fe_4$ phases distributed between the grains distributed between the grains, resulting in the formation of dislocations [46]. However, stress concentrations can be caused by the coarse $Al_{13}Fe_4$ phases in the AA8176 alloy without Y addition, which have a negative impact on the mechanical properties of the AA8176 alloys. When the Y addition was increased to 0.5 wt.%, the morphology of the $Al_{13}Fe_4$ phases was transformed into short rod-like and particulate with an average length of 2.65 μm . Consequently, the stress concentration during plastic deformation is effectively mitigated by this refinement for $Al_{13}Fe_4$ phases. Meanwhile, the number of secondary phases in the alloy matrix is further increased by the formation of $Al_{10}Fe_2Y$ phases, which grow around the $Al_{13}Fe_4$ phases. The mechanical properties of the AA8176 alloy with 0.5wt.%Y are enhanced by this dual effect. When the Y addition exceeded the optimal content of 0.5 wt.%, no further enhancement in the adsorption effect of Y on $Al_{13}Fe_4$ phases was observed. However, the nucleation and growth temperature of the $Al_{10}Fe_2Y$ phases was increased by the excessive addition of Y. The Y atoms that would otherwise inhibit the growth of $Al_{13}Fe_4$ are consumed by the growth of the $Al_{10}Fe_2Y$ phases, eventually leading to the formation of coarse $Al_{13}Fe_4$ and $Al_{10}Fe_2Y$ phases, which consequently results in the degradation of mechanical properties.

 doi:10.20944/preprints202512.1715.v1

Secondly, the SDAS of the AA8176 alloys was significantly reduced by the addition of Y, leading to a more refined microstructure. Secondly, the addition of Y significantly reduces the SDAS of the AA8176 alloys, resulting in a more refined microstructure. Generally, finer grains lead to a higher density of grain boundaries. Dislocation movement is effectively hindered and dislocation pile-up is induced by this increased boundary density, resulting in a significant improvement in the strength of the AA8176 alloys.

Gerbe et al. [47] proposed that in hypoeutectic alloys, the dendritic regions are regarded as behaving similarly to grain boundaries in polycrystalline alloys, since the eutectic zones between dendrites are traversed by slip planes. The SDAS is considered analogous to grain size in the Hall-Petch relationship, whereby a reduction in the mean free path of dislocation motion during plastic deformation is produced by smaller dendritic regions, thus further enhancing the strength of the AA8176 alloys.

5. Conclusions

1. For the as-cast AA8176 alloys, an optimal microstructure was achieved by the addition of 0.5 wt.% Y. In the unmodified AA8176, the microstructure is predominantly composed of the α-Al phases and the eutectic structure. The SDAS of α-Al phases was measured to be approximately 31.33 μm, and a needle-like morphology with an average length of 10.01 μm was exhibited by the iron-rich phases. In contrast, after the addition of 0.5 wt.% Y, the SDAS of the alloy was decreased to 20.24 μm, and the iron-rich phases were transformed into short rod-like and particulate forms with an average length of 2.65 μm. With the Y content exceeded 0.5wt.%, no significant change in the SDAS of α-Al phases was observed, while an increase in both the number and average size of the iron-rich phases occurred.

2. In the unmodified AA8176 alloy, the iron-rich phases consist of $Al_{13}Fe_4$ phases. The refinement of the $Al_{13}Fe_4$ phases is primarily attributed to the adsorption effect of Y atoms around these phases. Microstructural observations revealed that small size $Al_{10}Fe_2Y$ ternary phases were attached to the surfaces of $Al_{13}Fe_4$ phases in the AA8176 alloy with 0.5wt.%Y content. When the Y content exceeded 0.5 wt.%, the coarse $Al_{10}Fe_2Y$ phases were formed. And a substantial consumption of Y atoms is caused by the growth of these $Al_{10}Fe_2Y$ phases, resulting in a weakening of the refinement effect.

3. With the Y content increased, a trend of initially increasing and then decreasing was exhibited by the mechanical properties of the cast AA8176 alloys. When the Y content was 0.5 wt.%, an optimal balance of strength and ductility was achieved, with tensile strength and elongation measured at 96.86 MPa and 23.1 %, respectively. The primary strengthening mechanism of the AA8176 alloys is attributed to the refinement in the morphology of iron-rich phases and reduction in the SDAS of α-Al matrix. When the Y content exceeded 0.5 wt.%, coarse $Al_{10}Fe_2Y$ phases were formed, and the refining effect was reduced. The deterioration in the mechanical properties of the alloy is attributed to both coarse $Al_{13}Fe_4$ phases and $Al_{10}Fe_2Y$ phases lead to worse mechanical properties of the alloy.

Author Contributions: Conceptualization, W.W. and C.L.; methodology, W.W.; formal analysis, W.W.; investigation, W.W., W.X. and Z.C.; resources, C.L. and M.Z.; data curation, W.W., W.X. and Z.C.; writing—original draft preparation, W.W.; writing—review and editing, W.W., C.L. and M.Z.; supervision, C.L. and M.Z.; funding acquisition, C.L. and M.Z. All authors have read and agreed to the published version of the manuscript.

Funding: This research was funded by National Natural Science Foundation of China under Grant No. 51672145, 52171229 and 51872034.

Data Availability Statement: The data presented in this study is available on request from the corresponding author. The data is not publicly available due to privacy restrictions.

Conflicts of Interest: The authors declare that they have no known competing financial interests or personal relationships that could have appeared to influence the work reported in this paper.

Abbreviations

 doi:10.20944/preprints202512.1715.v1

The following abbreviations are used in this manuscript:

MDPI	Multidisciplinary Digital Publishing Institute
DOAJ	Directory of open access journals
TLA	Three letter acronym
LD	Linear dichroism

References

1. Medvedev A, Zhukova O, Enikeev N, et al. The effect of casting technique and severe straining on the microstructure, electrical conductivity, mechanical properties and thermal stability of the Al–1.7 wt.% Fe alloy. *Materials*, **2023**, 16(8): 3067. https://doi.org/10.3390/ma16083067
2. Zhao Q, Qian Z, Cui X, et al. Optimizing microstructures of dilute Al–Fe–Si alloys designed with enhanced electrical conductivity and tensile strength. *Journal of Alloys and Compounds*, **2015**, 650: 768-776. https://doi.org/10.1016/j.jallcom.2015.08.052
3. S Meignanamoorthy M, Ravichandran M, Mohanavel V, et al. Microstructure, mechanical properties, and corrosion behavior of boron carbide reinforced aluminum alloy (Al-Fe-Si-Zn-Cu) matrix composites produced via powder metallurgy route. *Materials*, **2021**, 14(15): 4315. https://doi.org/10.3390/ma14154315
4. Trink B, Weißensteiner I, Uggowitzer P J, et al. High Fe content in Al-Mg-Si wrought alloys facilitates excellent mechanical properties. *Scripta Materialia*, **2022**, 215: 114701. https://doi.org/10.1016/j.scriptamat.2022.114701
5. Wang X, Guan R G, Wang Y, et al. Mechanistic understanding on the evolution of nanosized Al_3Fe phase in Al–Fe alloy during heat treatment and its effect on mechanical properties. *Materials Science and Engineering: A*, **2019**, 751: 23-34. https://doi.org/10.3390/ma14154315
6. Que Z, Fang C, Mendis C L, et al. Effects of Si solution in θ-Al13Fe4 on phase transformation between Fe-containing intermetallic compounds in Al alloys. *Journal of Alloys and Compounds*, **2023**, 932: 167587. https://doi.org/10.1016/j.jallcom.2022.167587
7. Chen J, Lengsdorf R, Henein H, et al. Microstructure evolution in undercooled Al–8 wt% Fe melts: Comparison between terrestrial and parabolic flight conditions. *Journal of alloys and compounds*, **2013**, 556: 243-251. https://doi.org/10.1016/j.jallcom.2012.11.182
8. Que Z, Wang Y, Mendis C L, et al. Understanding Fe-containing intermetallic compounds in Al alloys: An overview of recent advances from the LiME research hub. *Metals*, **2022**, 12(10): 1677. https://doi.org/10.3390/met12101677
9. Zhao Y, Zhang W, Song D, et al. Nucleation and growth of Fe-rich phases in Al-5Ti-1B modified Al-Fe alloys investigated using synchrotron X-ray imaging and electron microscopy. *Journal of Materials Science & Technology*, **2021**, 80: 84-99. https://doi.org/10.1016/j.jmst.2020.12.011
10. Nayak S S, Chang H J, Kim D H, et al. Formation of metastable phases and nanocomposite structures in rapidly solidified Al–Fe alloys. *Materials Science and Engineering: A*, **2011**, 528(18): 5967-5973. https://doi.org/10.1016/j.msea.2011.04.028
11. Nayak S S, Wollgarten M, Banhart J, et al. Nanocomposites and an extremely hard nanocrystalline intermetallic of Al–Fe alloys prepared by mechanical alloying. *Materials Science and Engineering: A*, **2010**, 527(9): 2370-2378. https://doi.org/10.1016/j.msea.2009.12.044
12. Lan Q, Le Q, Liao Q, et al. Effect of AC magnetic field on Al3Fe phase by measuring thermoelectric power. *Materials Chemistry and Physics*, **2018**, 214: 383-390. https://doi.org/10.1016/j.matchemphys.2018.04.105
13. Duchaussoy A, Sauvage X, Edalati K, et al. Structure and mechanical behavior of ultrafine-grained aluminum-iron alloy stabilized by nanoscaled intermetallic particles. *Acta Materialia*, **2019**, 167: 89-102. https://doi.org/10.1016/j.actamat.2019.01.027
14. Medvedev A, Murashkin M, Enikeev N, et al. Influence of morphology of intermetallic particles on the microstructure and properties evolution in severely deformed Al-Fe alloys. *Metals*, **2021**, 11(5): 815. https://doi.org/10.3390/met11050815
15. Song D, Zhao Y, Jia Y, et al. Synergistic effects of Mn and B on iron-rich intermetallic modification of recycled Al alloy. *Journal of Materials Research and Technology*, **2023**, 24: 527-541. https://doi.org/10.1016/j.actamat.2019.01.027

 doi:10.20944/preprints202512.1715.v1

16. Watanabe Y, Mihara-Narita M, Sato H. Grain refinement of cast aluminum by heterogeneous nucleation site particles with high lattice matching. *Materials Transactions*, **2023**, 64(6): 1083-1097. https://doi.org/10.2320/matertrans.MT-L2022026
17. Qin L, Tang P, Meng S. Effect of Ni addition on the microstructure, conductivities and mechanical properties of as-cast Al-Fe alloys. *Journal of Alloys and Compounds*, **2024**, 986: 174160. https://doi.org/10.1016/j.jallcom.2024.174160
18. Song X, Gao M, Yang B, et al. Modification and refinement of Fe-containing phases, mechanical properties and strengthening mechanisms in Al–Fe alloys via Cr alloying and continuous rheo-extrusion. *Materials Science and Engineering: A*, **2022**, 850: 143557. https://doi.org/10.1016/j.msea.2022.143557
19. Xu H, Jia H, Ji Z, et al. Effect of La content on microstructure, tensile properties, and electrical conductivity of cast Al-Mg-Si-xLa alloys. *China Foundry*, **2025**: 1-10. https://link.springer.com/article/10.1007/s41230-025-4101-6
20. Liao H C, Liu Y, Lü C L, et al. Effect of Ce addition on castability, mechanical properties and electric conductivity of Al–0.3 Si–0.2 Mg alloy. *International Journal of Cast Metals Research*, **2015**, 28(4): 213-220. https://doi.org/10.1179/1743133615Y.0000000002
21. Mahmoud M G, Mosleh A O, Mohamed M S, et al. The impact of Ce-containing precipitates on the solidification behavior, microstructure, and mechanical properties of Al-6063. *Journal of Alloys and Compounds*, **2023**, 948: 169805. https://doi.org/10.1016/j.jallcom.2023.169805
22. Liang Y H, Shi Z M, Li G W, et al. Effects of Er addition on the crystallization characteristic and microstructure of Al-2wt% Fe cast alloy. *Journal of Alloys and compounds*, **2019**, 781: 235-244. https://doi.org/10.1016/j.jallcom.2018.12.063
23. Li Y, Yu Q, Chen F, et al. Effect of Sc on Al3Fe phase and mechanical properties of as-cast AA5052 aluminum alloy. *China Foundry*, **2024**, 21(3): 257-264. https://link.springer.com/article/10.1007/s41230-024-3083-0
24. Dai K, Ye J, Wang Z, et al. Effects of Sc and Zr addition on the solidification and mechanical properties of Al–Fe alloys. *Journal of Materials Research and Technology*, **2022**, 18: 112-121. https://doi.org/10.1016/j.jmrt.2022.02.070
25. Mo L, Jiang M, Zhou X, et al. Modification mechanisms of hypereutectic Al-Fe alloys treated by Sm/Yb addition: experiments and first-principles calculations. *Journal of Alloys and Compounds*, **2023**, 948: 169786. https://doi.org/10.1016/j.jallcom.2023.169786
26. Sahin H, Dispinar D. Effect of rare earth elements erbium and europium addition on microstructure and mechanical properties of A356 (Al–7Si–0.3 Mg) alloy. *International Journal of Metalcasting*, **2023**, 17(4): 2612-2621. https://link.springer.com/article/10.1007/s40962-023-01060-3
27. Luo S X, Shi Z M, Li N Y, et al. Crystallization inhibition and microstructure refinement of Al-5Fe alloys by addition of rare earth elements. *Journal of Alloys and compounds*, **2019**, 789: 90-99. https://doi.org/10.1016/j.jallcom.2019.03.071
28. Pang N, Shi Z, Wang C, et al. Modification mechanisms of the primary Al13Fe4 phase in hypereutectic Al–Fe alloys by La element: Experiments and first–principles study. *Journal of Crystal Growth*, **2025**, 659: 128136. [CrossRef]
29. Pang N, Shi Z, Wang C, et al. Doping and adsorption mechanism of the element Y modifying the primary $Al_{13}Fe_4$ phase in hypereutectic Al–Fe alloys from first-principles. *CrystEngComm*, **2021**, 23(21): 3802-3811. https://pubs.rsc.org/en/content/articlelanding/2021/ce/d1ce00238d/unauth
30. Mao G, Liu S, Wu Z, et al. The effects of Y on primary α-Al and precipitation of hypoeutectic Al-Si alloy. *Materials Letters*, **2020**, 271: 127795. https://doi.org/10.1016/j.matlet.2020.127795
31. Mao G, Yan H, Zhu C, et al. The varied mechanisms of yttrium (Y) modifying a hypoeutectic Al–Si alloy under conditions of different cooling rates. *Journal of Alloys and Compounds*, **2019**, 806: 909-916. https://doi.org/10.1016/j.jallcom.2019.07.107
32. Ding W, Zhao X, Chen T, et al. Effect of rare earth Y and Al–Ti–B master alloy on the microstructure and mechanical properties of 6063 aluminum alloy. *Journal of Alloys and Compounds*, **2020**, 830: 154685. https://doi.org/10.1016/j.jallcom.2020.154685

33. Liu J, Wu Q, Yan H, et al. Effect of trace yttrium addition and heat treatment on the microstructure and mechanical properties of as-cast ADC12 aluminum alloy. *Applied Sciences*, **2018**, 9(1): 53. https://doi.org/10.3390/app9010053
34. Wan B, Chen W, Liu L, et al. Effect of trace yttrium addition on the microstructure and tensile properties of recycled Al–7Si–0.3 Mg–1.0 Fe casting alloys. *Materials Science and Engineering: A*, **2016**, 666: 165-175. https://doi.org/10.1016/j.msea.2016.04.036
35. Jiang H, Li S, Zhang L, et al. The influence of rare earth element lanthanum on the microstructures and properties of as-cast 8176 (Al-0.5 Fe) aluminum alloy. *Journal of Alloys and Compounds*, **2021**, 859: 157804. https://doi.org/10.1016/j.jallcom.2020.157804
36. Nemati N, Emamy M. Evaluating Microstructure and High-Temperature Shear Behavior of Hot Extruded Al-Al13Fe4 Nanocomposite. *MATERIALS TRANSACTIONS*, **2016**, 57(8): 1236-1245. https://doi.org/10.2320/matertrans.MG201605
37. Waerenborgh J C, Salamakha P, Sologub O, et al. Y–Fe–Al ternary system: partial isothermal section at 1070 K: Powder X-ray diffraction and Mössbauer spectroscopy study. *Journal of alloys and compounds*, **2001**, 323: 78-82. https://doi.org/10.1016/S0925-8388(01)00990-2
38. da Silva Leal J R, Saldanha F E, Ganju E, et al. Effect of cooling rate on AlFe primary and eutectic phase growth evolution in an Al-2Fe-1Mn alloy. *Journal of Alloys and Compounds*, **2025**, 1010: 177870. https://doi.org/10.1016/j.jallcom.2024.177870
39. Mao F, Li J, Yan G, et al. Effect of Eu on the silicon phase in Al-40Zn-5Si alloys. *Journal of Alloys and Compounds*, **2017**, 722: 116-130. https://doi.org/10.1016/j.jallcom.2017.06.086
40. Wang M, Knezevic M, Chen M. Effects of Fe content on microstructure and mechanical properties of Al-Y eutectic alloys. *Materials Science and Engineering: A*, **2023**, 863: 144558. https://doi.org/10.1016/j.msea.2022.144558
41. Hume-Rothery W, Raynor G V. The Structure of Metals and Alloys. *Nature*, **1936**, 138: 7–8. https://www.nature.com/articles/138007a0#citeas
42. Li B, Wang H, Jie J, et al. Effects of yttrium and heat treatment on the microstructure and tensile properties of Al–7.5 Si–0.5 Mg alloy. *Materials & Design*, **2011**, 32(3): 1617-1622. https://doi.org/10.1016/j.matdes.2010.08.040
43. Mao F, Yan G, Xuan Z, et al. Effect of Eu addition on the microstructures and mechanical properties of A356 aluminum alloys. *Journal of Alloys and Compounds*, **2015**, 650: 896-906. https://doi.org/10.1016/j.jallcom.2015.06.266
44. Zheng Q, Zhang L, Jiang H, et al. Effect mechanisms of micro-alloying element La on microstructure and mechanical properties of hypoeutectic Al-Si alloys. *Journal of Materials Science & Technology*, **2020**, 47: 142-151. https://doi.org/10.1016/j.jmst.2019.12.021
45. He J, Liao X, Lan X, et al. Annealed Al-Cr coating: A hard anti-corrosion coating with grain boundary modification effect for Nd-Fe-B magnets. *Journal of Alloys and Compounds*, **2021**, 870: 159229. https://doi.org/10.1016/j.jallcom.2021.159229
46. Fuller C B, Seidman D N, Dunand D C. Mechanical properties of Al (Sc, Zr) alloys at ambient and elevated temperatures. *Acta materialia*, **2003**, 51(16): 4803-4814. https://doi.org/10.1016/S1359-6454(03)00320-3
47. Gerbe S, Krupp U, Michels W. Influence of secondary dendrite arm spacing (SDAS) on the fatigue properties of different conventional automotive aluminum cast alloys. *Fracture and Structural Integrity*, **2019**, 13(48): 105-115. https://doi.org/10.3221/IGF-ESIS.48.13